PAPER • OPEN ACCESS

Bound states in the continuum and exceptional points in dielectric waveguide equipped with a metal grating

To cite this article: Ryo Kikkawa *et al* 2020 *New J. Phys.* **22** 073029

New Journal of Physics
The open access journal at the forefront of physics

Deutsche Physikalische Gesellschaft DPG
IOP Institute of Physics

Published in partnership with: Deutsche Physikalische Gesellschaft and the Institute of Physics

OPEN ACCESS

RECEIVED
22 January 2020

REVISED
7 May 2020

ACCEPTED FOR PUBLICATION
29 May 2020

PUBLISHED
21 July 2020

PAPER

Bound states in the continuum and exceptional points in dielectric waveguide equipped with a metal grating

Ryo Kikkawa, Munehiro Nishida and Yutaka Kadoya

Graduate School of Advanced Sciences of Matter, Hiroshima University, 1-3-1 Kagamiyama, Higashihiroshima, Hiroshima 7398530, Japan

E-mail: mnishida@hiroshima-u.ac.jp

Keywords: bound states in the continuum, dielectric waveguide, grating

Abstract

Bound states in the continuum (BICs) and exceptional points (EPs) have been the subjects of recent intensive research as they exhibit exotic phenomena that are significant for both fundamental physics and practical applications. We investigated the emergence of the Friedrich–Wintgen (FW) type BIC and the EP in a dielectric waveguide comprising a metal grating, focusing on their dependence on the grating thickness. The BIC emerges at a branch near the anti-crossing formed of the two waveguide modes, for a grating of any thickness. With the grating-thickness change, the anti-crossing gap varies and the branch at which the BIC appears flips. We show that, when the slit is single mode, the BIC appears in the vicinity of the crossing between the two waveguide modes in the empty-lattice (zero slit-width) limit, while the results satisfy the criteria for the branch at which the BIC appears in the previous reports. In addition, we find that the EP appears near the BIC in the same device only on selecting the grating thickness. The BIC and EP in the dielectric waveguide comprising a metal grating, particularly with such tunability, are expected to result in the development of functional and high-performance photonic devices in addition to being a platform for the fundamental research of non-Hermitian systems.

1. Introduction

Resonant oscillations in open resonator systems (the system that possesses the radiation port to the far region) normally decay with time because of the radiative dissipation of the energy. Even in open systems, however, purely bound states can exist when some requisite conditions are fulfilled. Such a non-decaying state in an open system is called a bound state in the continuum (BIC) [1, 2] and was originally discussed in quantum mechanics in 1929 by von Neumann and Wigner [3]. Reports on BICs in optics started to appear in 2000s [4–6], though the word 'BIC' was not used before 2008 [7, 8]. After some years, experimental demonstrations on photonic BICs have been reported, first in a proof-of-principle manner [9, 10] and then in more practical photonic device [11]. In real devices, a complete BIC may not be realized, because of the finiteness of the size or the imperfection of the structure [1]. Nevertheless, because of the strong light trapping, the Q-value of the resonance can become very high near the BIC point or at the quasi-BIC [12] including the cases of avoided crossing in localized dielectric structures [13]. Relying on the high-Q resonances, applications such as optical modulators [14], single mode lasers [15, 16], high-efficiency nonlinear photonics [17–20], and sensors [21, 22] have been demonstrated. BICs can be categorized into several types based on their physical origin [1]. Among them, two types of BIC, the symmetry-protected BIC [23] and accidental or Friedrich–Wintgen (FW) BIC [24], have been mostly investigated. The former originates from the incompatibility of the symmetry between the resonant mode and external radiation and appears at highly symmetric points such as the Γ point in the reciprocal space of the periodic structure. The latter is formed by the destructive interference between the radiation from the resonant modes [1, 25],

where the symmetry is generally not required and can appear at a point of no symmetry in the reciprocal space.

When the two relevant modes constituting the FW–BIC interact in the near field, the dispersion of the modes anti-crosses and the BIC lies on one of the split branches [4, 24, 26–31]. From a view point of device design for applications, it is important to know the position at which the BIC appears. Though it can be predicted formally by the theory of Friedrich and Wintgen [24], the correspondence to the parameters in specific device structures had not been discussed in optical devices. In our recent report [32], we presented that, in a dielectric waveguide connected with the far field through a metal grating, the branch on which the BIC appears depends on the polarization of the mode, which is explained by the difference in the parameter describing the coupling phase of the modes with the external radiation, in a consistent manner with the original theory of Friedrich and Wintgen [24]. In the present article, we show that the branch at which the FW–BIC emerges also depends on the grating thickness. On carefully inspecting the dispersion relation, we found that the position at which the BIC appears is fixed in the vicinity of the crossing of the original waveguide modes, while the coupled resonant modes of the entire system move owing to the change in the grating thickness, thus resulting in the flipping of the BIC branch. We also show that the criteria discussed in our previous paper for the branch at which the BIC appears still hold. In addition, we observed that the magnitude of the anti-crossing gap and hence, the internal (near field) coupling, varies with the change in the grating thickness.

In parallel, with the Hamiltonian of essentially the same form as that describes a system exhibiting the FW–BIC, the eigen-solutions of non-Hermitian systems have been intensively investigated with an emphasis on the presence and the influence of exceptional points (EPs) at which the eigen-solutions (resonant modes) formed from more than one oscillator with the mutual coupling coalesce [33, 34]. In optics and photonics, EPs in active or passive parity-time (PT) symmetric structures as well as those in non-PT symmetric structures have attracted a significant amount of interest [35, 36] as such systems exhibit various exotic as well as practically important phenomena at or around the EP. For example, asymmetric mode switching [37], directional omni-polarizer [38], laser mode selection [39–41], unidirectional invisibility or reflectionlessness [42], directional total absorption [43], loss-induced transparency [44], polarization control [45] and enhancement of Sagnac sensitivity [46, 47] have been proposed and/or demonstrated. They are expected to lead to a new paradigm of optical systems.

Though many of the reports on EPs have dealt with the case of no external (radiation) coupling, which is the origin of the FW–BIC, the EP is expected to appear even with the radiation coupling [34], and hence, the BIC and EP are closely located in the parameter space [48]. In the last part of this article, we show that the EP can indeed be realized near the BIC point in our device, where the tuning of the internal coupling with the grating thickness plays a significant role. The continuous controllability of the system with the use of such an additional parameter is expected to encourage experimental investigations and the application of the BIC- and EP-related phenomena in optics and photonics [49].

2. Device structure and the methods of analysis

The system considered in this study is a dielectric waveguide sandwiched by a metal grating and optically thick backing metal, which is essentially the same structure as that considered in our previous paper [32], as shown in figure 1. In this paper, we only vary the grating thickness h_{metal} and fix the other parameters. We consider the region of the wavelength where only the 0th order wave is radiative in the air region. For the permittivity of the gold, unless otherwise stated, the Drude–Lorentz model fitting the reported experimental data [50] was used. In some cases, however, we eliminated the imaginary part of the permittivity to neglect the loss and simplify the theoretical analysis. We will specify the elimination when it is done. We consider a case where a *P*-polarized wave is incident from the air region. Owing to the backing metal, the incident light is totally reflected unless it is absorbed due to the ohmic loss at the metal surface. Strong absorption occurs when the incident light excites the resonant mode, which comprises the waveguide modes in the dielectric region with a modification of the slit-induced internal and external (radiation) coupling. Although a specific application is not supposed here, the device parameters are chosen to maintain the link to our previous reports [32, 54], where the refractive index of the dielectric layer $n_{\mathrm{diel}} = 3.6$ was determined with semiconductor devices in mind. The structure considered here can be fabricated by a wafer bonding technique used, for example, in the fabrication of quantum cascade lasers [51].

The dominant waveguide modes for the situation considered in this paper are the first (lowest) and second transverse magnetic (TM) modes, TM_0 and TM_1, respectively, in the metal-dielectric-metal (MIM) structure. The higher order modes are well separated for the optical thickness of the dielectric layer and the wavelength range considered. Also, the coupling between the TM modes and the transverse electric (TE)

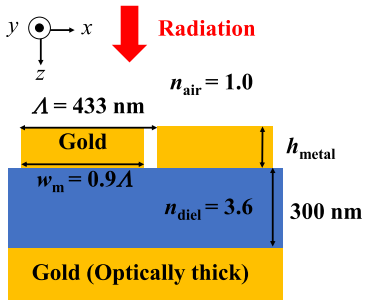

Figure 1. Cross-sectional structure of the device considered in this work.

modes does not occur for the waves propagating perpendicularly to the grating. Therefore, the effect of the TE and higher TM modes are safely neglected here.

For the analysis of the electromagnetic field and the resonant (eigen) mode in the device, a spatial coupled-mode method (CMM) [52] was used. In the CMM, the wave propagation in the grating layer was described by that in a slit sandwiched by the nearby metal bars and the modes were calculated taking into account the permittivity of gold [53, 54]. For the slit width of 43.3 nm considered here, only one propagating mode is present. In addition, a temporal coupled-mode theory (TCMT) [55, 56] was used to analyze the response obtained by the CMM. It should be noted that the CMM and TCMT are essentially different from each other; the former is a numerical solver of the EM field based on Maxwell's equations, while the latter is an equation that describes the motion of the oscillators corresponding, in the present case, to the original TM_0 and TM_1 modes with mutual internal and external coupling.

3. Absorption spectra and the resonant mode of the system

Figure 2 shows the dispersion relation of the absorption for the wave incident from the air region in the gray-scale maps for the four cases of the grating thickness h_{metal}. The solid lines on the absorption map indicate the wavelength corresponding to the real part of the resonant mode frequency. It can be observed that the high-absorption bands appear along the resonant modes. As mentioned above, each resonant mode can be assigned to an originating MIM mode, except in the case of the anti-crossing region wherein the modes are mixed by the slit. In all the cases of the grating thickness, as indicated by the dashed circles, the absorption disappears locally near the anti-crossing. This behavior is a signature of the emergence of the BIC. The imaginary part of the resonant mode frequency is depicted in the lower panel for each h_{metal} with the same colors for each branch as those used for the real part. In the calculation of the resonant modes, the imaginary part of the metal permittivity was set to zero such that the imaginary part of the resonant mode frequency is only due to the radiation loss. The disappearance of the absorption corresponds to the vanishing imaginary part, which confirms that the disappeared mode is indeed the BIC.

There are two remarkable features of the absorption map and resonant mode dispersion. First, the magnitude of the anti-crossing gap depends on h_{metal}. With the increase in h_{metal}, the gap first becomes small and almost diminishes for $h_{metal} \sim 275$ nm. The gap then reappears with a further increase in h_{metal}. Second, the branch at which the BIC appears changes as h_{metal} crosses ~ 275 nm, where the gap shrinkage occurs. The BIC appears on the lower branch for $h_{metal} < 275$ nm and on the higher branch for $h_{metal} > 275$ nm. In the following, we discuss these features in detail, in the order of 1) the position and branch of the BIC and 2) the variation of the anti-crossing gap in sections 4 and 5, respectively.

4. Position of the BIC

4.1. The position of the BIC in terms of the empty lattice mode

Here, we first discuss the position and the branch of the BIC. In figure 3, we present a magnified view of figure 2 near the anti-crossing. The position of the BIC is indicated by the dashed circles. As mentioned above, the BIC appears on the lower (upper) branch for $h_{metal} < 275 (> 275)$ nm. For $h_{metal} = 275$ nm, the anti-crossing disappears and the BIC appears in the vicinity of crossing point. On observing the figure more closely, we notice that the position of the BIC is not moved by the change in h_{metal}. The broken lines plotted in the figures are the empty lattice TM_0 and TM_1 waveguide modes, which were obtained by folding the dispersion curves of these modes in the MIM waveguide with flat metals (no slit) into the first Brillouin zone. Interestingly and importantly, it can be clearly observed that the BIC is always located in the vicinity

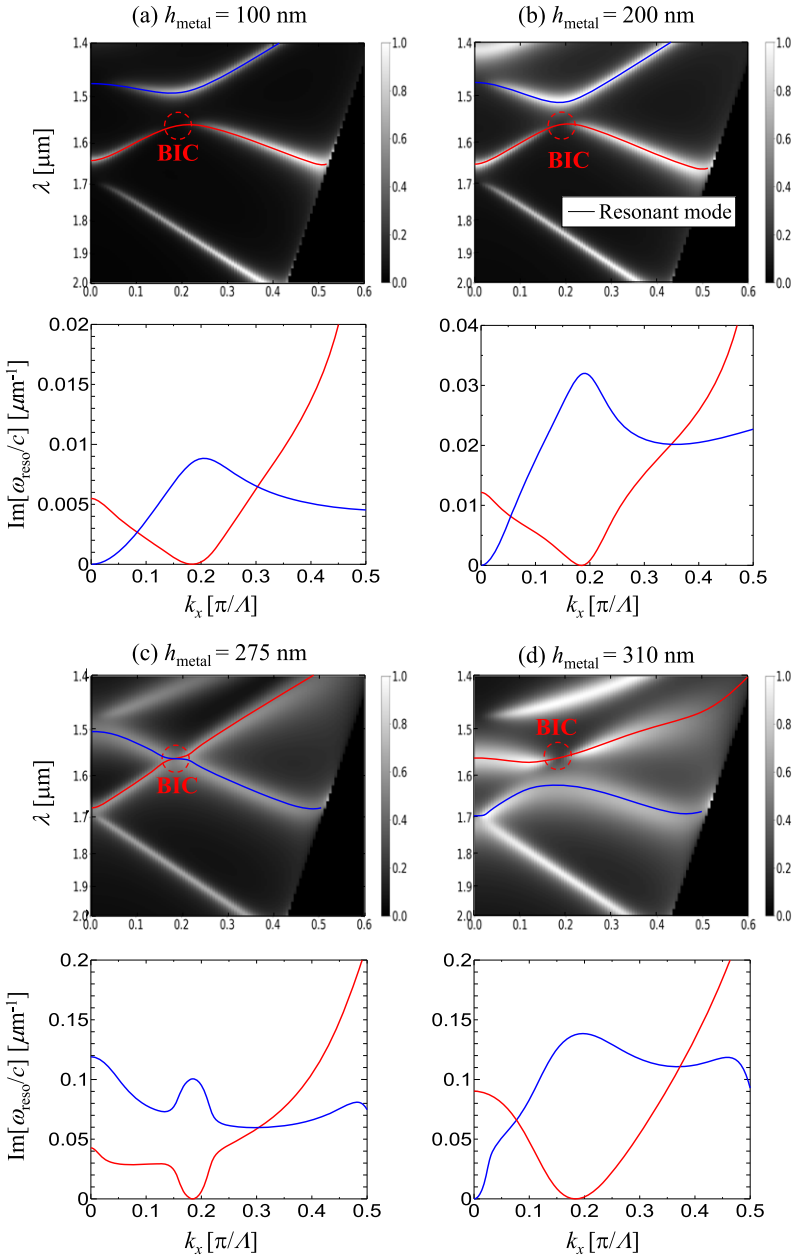

Figure 2. Dispersion relation of the absorption and the resonant mode for the four cases of h_{metal}: (a) 100 nm, (b) 200 nm, (c) 275 nm and (d) 310 nm. In the upper panel, the absorption is depicted by the gray scale along with the wavelength corresponding to the real part of the resonant-mode frequency indicated by the blue and red lines. In the lower panel, the imaginary part of the angular frequency of the resonant mode is plotted using the same color as that used for the same branch in the real part. The frequency was normalized by the speed of the light c in vacuum. It should be noted that the wavelength is given in the inverted scale (linear in frequency). The dashed circles indicate the position of the BIC.

of the crossing point of the two empty lattice bands, which does not move with the change in the grating thickness. Therefore, the branch inversion of the BIC that is observed in figure 2 is understood to be a result of the movement of the leaky mode associated with the change in the grating thickness over the BIC point, which is fixed in the vicinity of the crossing of the empty lattice dispersion.

The appearance of the BIC in the vicinity of the crossing point of the empty lattice bands can be explained using the CMM as follows. For the BIC solution, the radiative fields in the air region become null owing to the nature of the BIC. It can be realized when the fields inside the slit are null, if the slit is single mode as in the present device. In such cases, the fields in the dielectric region satisfy the same relation at the slit/waveguide interface as that of the empty lattice MIM modes, which means that the fields inside the dielectric region are those of the empty lattice modes when the BIC occurs. It should be mentioned that the explanation described above is the over-simplified picture only exact within the CMM treatment. As we discuss in appendix A, even when the higher order slit modes do not exist, slit-mode-like extended surface modes should exist and produces a slight discrepancy between the BIC position and the crossing point.

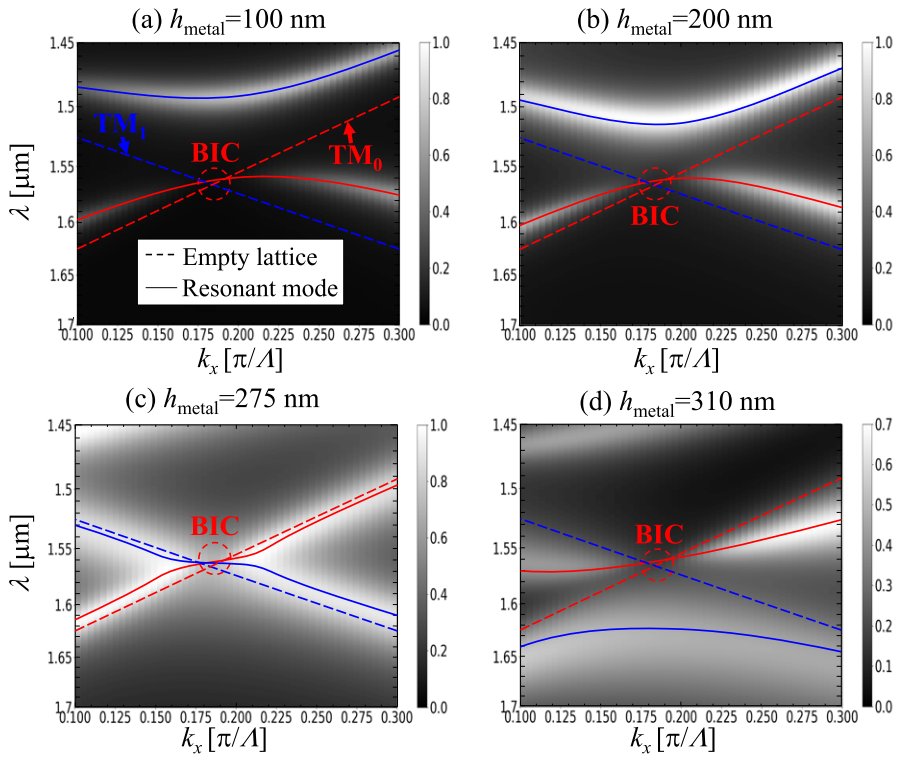

Figure 3. Magnified view of the absorption map shown in figure 2. The dashed circles, solid lines and dashed lines indicate the position of the BIC, dispersion of the resonant modes and empty lattice bands, respectively.

As another method of understanding the system, we calculated the reflection coefficient ρ_{diel} for the wave approaching the slit/dielectric interface from the infinitely thick grating as schematically depicted in figure 4 (a). Figure 4(c) shows the dispersion of $|\rho_{diel}|$ along with the empty lattice bands (indicated by dashed lines). It can be observed that the anti-crossing of the bands and the BIC occurs and that the BIC is located in the vicinity of the crossing of the empty lattice band, which is not affected by the grating. Then let us elucidate the role of the finite thickness of the grating. Indicated by the black solid line in figure 4(d) is $\arg(\rho_{diel})$ as a function of the wavelength for $k_x = 0.185\ [\pi/\Lambda]$, where the BIC emerges at $\lambda = 1563$ nm. It should be noted that $\arg(\rho_{diel})$ is affected only by the radiative mode because the BIC mode is not coupled to the slit as mentioned above. The red dashed line is $|\rho_{diel}|$. Between the dips in $|\rho_{diel}|$, which correspond to the coupled TM$_0$–TM$_1$ mode at approximately 1500 nm and uncoupled TM$_0$ mode at approximately 1800 nm, $\arg(\rho_{diel})$ varies gradually from 2π to 0. The wavelength of the BIC λ_{BIC} is indicated by the vertical dotted line. Now, let us hypothesize that the solution of the radiative mode of the entire system with a grating of finite thickness can be viewed as the Fabry–Perot (FP) resonance for the wave propagating in the slit, which is given by

$$\arg(\rho_{air}) + \arg(\rho_{diel}) + 2\beta_{slit}h_{metal} = 2\pi m, \tag{1}$$

where $\arg(\rho_{air})$ is the phase of the reflection at the slit/air interface (see figure 4(b)), β_{slit} is the propagation constant in the slit and m is an integer. The blue, green and orange lines in figure 4(d) indicate the value of $\arg(\rho_{diel})$ required to satisfy equation (1) for $h_{metal} = 200$, 275 and 310 nm, respectively. Hence, the point at which the line for each h_{metal} crosses $\arg(\rho_{diel})$ (indicated by the black circles) provides the wavelength that satisfies equation (1). For $h_{metal} = 200$ nm, the wavelength of the crossing is shorter than λ_{BIC}. This corresponds to figure 3(b) where the BIC is located on the longer-wavelength branch. For $h_{metal} = 275$ nm, the crossing is located near λ_{BIC}, which corresponds to figure 3(c). Then, for $h_{metal} = 310$ nm, the wavelength of the crossing is greater than λ_{BIC}, which corresponds to figure 3(d). It can be observed that the wavelength of the radiative mode in figure 3 at $k_x = 0.185\ [\pi/\Lambda]$, where the BIC emerges, is predicted very well, which justifies the hypothesis and that the thickness h_{metal} of the grating can be said to determine the wavelength that satisfies the FP condition in the slit for the radiative (non-BIC) solution. It should be mentioned again that the discussions presented here are valid for the case in which the wave propagation in the slit is in the single mode or only one mode is dominating.

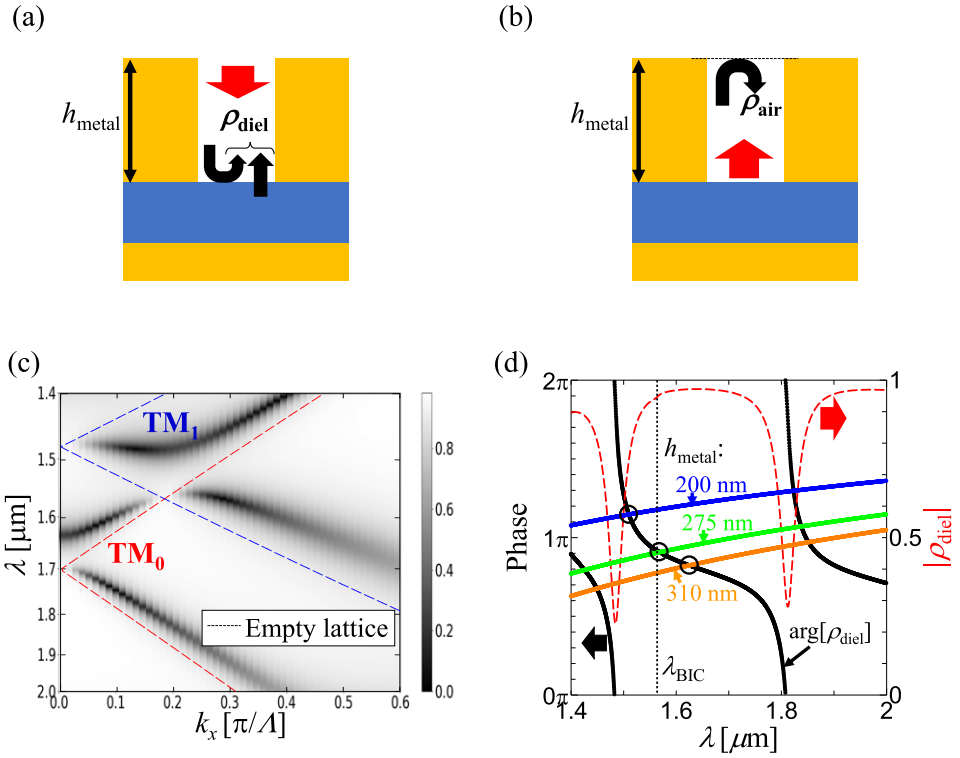

Figure 4. (a) Schematic showing the reflection coefficient ρ_{diel} at the slit/dielectric interface for the slit mode. (b) Schematic showing the reflection coefficient ρ_{air} at the slit/air interface for the slit mode. (c) $|\rho_{diel}|$ as a function of k_x and the wavelength depicted in gray scale. The empty lattice bands of the waveguide are superimposed by the dashed lines. (d) Amplitude (black solid line) and phase (red dashed line) of ρ_{diel} at $k_x = 0.185[\pi/\Lambda]$ for which the BIC appears. The blue, green and orange lines indicate the value of arg(ρ_{diel}) required to satisfy equation (1) for the cases of $h_{metal} = 200$, 275 and 310 nm, respectively. The solid circle indicates the intersection of these lines and arg(ρ_{diel}), which gives the FP resonance.

4.2. Temporal coupled-mode theory appropriate for the present system

The response of the present device can be analyzed using TCMT [32] for the two resonators corresponding to the empty-lattice TM$_0$ and TM$_1$ modes with the internal and external coupling. The time evolution of these two resonators $\mathbf{a}^{\mathrm{T}} = (a_1, a_2)$ driven by an external field s_+ with a coupling coefficient $\mathbf{D}$ can be written as

$$\frac{\mathrm{d}}{\mathrm{d}t}\mathbf{a} = -\mathrm{i}\{\mathbf{\Omega} - \mathrm{i}(\mathbf{\Gamma}_i + \mathbf{\Gamma}_e)\}\mathbf{a} + \mathbf{D}^{\mathrm{T}} s_+, \tag{2}$$

where the matrices $\mathbf{\Omega}$, $\mathbf{\Gamma}_i$ and $\mathbf{\Gamma}_e$ represent the eigenfrequencies with internal coupling, internal loss and radiation loss, respectively. Though the framework is essentially the same as that in a previous study [32], to analyze the present system, it is necessary to modify $\mathbf{\Omega}$ in order to keep the BIC solutions fixed in the vicinity of the degenerate point of the two basis modes. As presented below, the matrix $\mathbf{\Omega}$ that satisfies this requirement is,

$$\mathbf{\Omega} = \begin{pmatrix} \tilde{\omega}_1 \equiv \omega_1 + p\alpha\sqrt{\dfrac{\gamma_{e1}}{\gamma_{e2}}} & \alpha \\ \alpha & \tilde{\omega}_2 \equiv \omega_2 + p\alpha\sqrt{\dfrac{\gamma_{e2}}{\gamma_{e1}}} \end{pmatrix}, \tag{3}$$

where $\omega_{1,2}$ and $\gamma_{e1,2}$ are the eigenfrequency and external (radiation) loss of modes 1 or 2, respectively; α is the internal coupling; and p is the phase difference between the two modes for coupling to the external field. Here, p has the value of either $+1$ or -1; $p = +1$ if the two modes are in phase (no phase difference) and $p = -1$ if the two modes are out of phase (π phase difference) [32]. The modification comprises the addition of $p\alpha\sqrt{\frac{\gamma_{e1}}{\gamma_{e2}}}$ and $p\alpha\sqrt{\frac{\gamma_{e2}}{\gamma_{e1}}}$ to the diagonal terms of $\mathbf{\Omega}$. The matrices

$$\mathbf{\Gamma}_e = \begin{pmatrix} \gamma_{e1} & \gamma_0 \\ \gamma_0 & \gamma_{e2} \end{pmatrix}, \quad \mathbf{D}^{\mathrm{T}} = \mathrm{e}^{\mathrm{i}\varphi_d} \begin{pmatrix} \sqrt{2\gamma_{e1}} \\ p\sqrt{2\gamma_{e2}} \end{pmatrix}, \tag{4}$$

where $\gamma_0 = p\sqrt{\gamma_{e1}\gamma_{e2}}$ represents the radiation coupling and φ_d is an arbitrary phase, are the same as before, and the matrix

$$\mathbf{\Gamma}_i = \begin{pmatrix} \gamma_{i1} & 0 \\ 0 & \gamma_{i2} \end{pmatrix}, \tag{5}$$

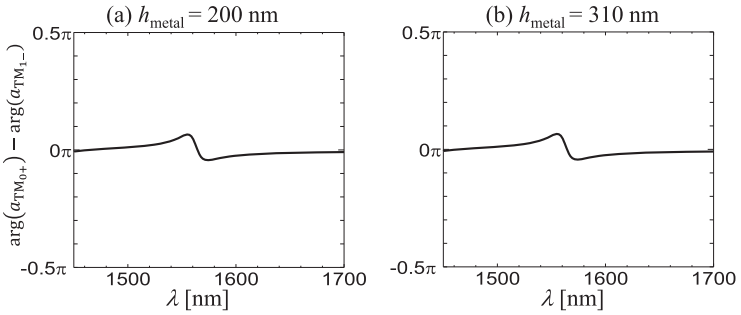

Figure 5. Phase difference between the amplitudes of the two waveguide modes near the anti-crossing ($k_x = 0.1839[\pi/\Lambda]$) as a function of wavelength. (a) $h_{\mathrm{metal}} = 200$ nm and (b) $h_{\mathrm{metal}} = 310$ nm.

where $\gamma_{i1,2}$ is the internal loss (in the metal in the present device) of each mode, was included in equation (2) for generalization. The expression for $\mathbf{D}$ and the off-diagonal terms of $\mathbf{\Gamma}_e$ are derived using the time-reversal symmetry and energy conservation law [56].

For the time dependence of $e^{-i\omega t}$, the eigenfrequencies of the resonant modes are obtained [24, 34, 57, 58] from equation (2) as the solution of

$$\{\omega - (\tilde{\omega}_1 - i\gamma_{t1})\}\{\omega - (\tilde{\omega}_2 - i\gamma_{t2})\} + (ip\alpha + \sqrt{\gamma_{e1}\gamma_{e2}})^2 = 0 \tag{6}$$

where $\gamma_{t1,2} = \gamma_{i1,2} + \gamma_{e1,2}$. The condition for one of the solutions being the BIC can be derived from equation (6), by assuming that one of the solutions is purely real [32]. On assuming $\gamma_{i1} = \gamma_{i2} = 0$ for simplicity, we obtain the condition

$$\omega_1 = \omega_2 \equiv \omega_0. \tag{7}$$

Then, the solutions are

$$\omega = \begin{cases} \omega_0 + p\alpha\left(\sqrt{\dfrac{\gamma_{e1}}{\gamma_{e2}}} + \sqrt{\dfrac{\gamma_{e2}}{\gamma_{e1}}}\right) - i(\gamma_{e1} + \gamma_{e2}) \\ \omega_0 \end{cases} . \tag{8}$$

The first solution is radiative (leaky) with the loss $\gamma_{e1} + \gamma_{e2}$ and the second solution is the BIC, which has no imaginary part. Thus, the formulation is confirmed to provide the BIC that always lies at the crossing point of the original eigenfrequencies, $\omega_0 = \omega_1 = \omega_2$. The behavior of the branch inversion of the BIC calculated using the TCMT developed in this section is shown in appendix B.

4.3. Prediction of BIC-branch in terms of $p\alpha$

In the preceding subsections, we showed that the BIC appears in the vicinity of the crossing point of the empty-lattice modes. In our previous report [32], we showed that the branch at which the BIC appears is determined by the sign of $p\alpha$. Herein, we show that the aforementioned rule still holds. In the TCMT analysis, as observed in equation (8), the branches at which the BIC appears are determined as follows:

$$p\alpha \quad \begin{cases} > 0 & (\text{lower branch}) \\ < 0 & (\text{upper branch}) \end{cases} , \tag{9}$$

as in the case without modification [32]. Therefore, we check sign($p\alpha$) for the cases of $h_{\mathrm{metal}} < 275$ nm and $h_{\mathrm{metal}} > 275$ nm, where the BIC appears at the upper and lower branches, respectively, as shown in figures 2 or 3.

The evaluation of sign$\{p\alpha\}$ was conducted in the same manner as before [32], i.e. by expanding the electromagnetic fields inside the dielectric waveguide of the empty-lattice waveguide modes. In the present case, the dominant modes are the right-propagating TM_0 and the left propagating TM_1 modes near the anti-crossing point. Sign(p) and sign(α) are then evaluated from the complex amplitude of each mode obtained in the expansion. Sign(p) is evaluated directly from the phase difference between the complex amplitudes. Figures 5(a) and (b) show the calculated phase difference at $k_x = 0.1839[\pi/\Lambda]$, which is slightly displaced from the point at which the BIC emerges, for $h_{\mathrm{metal}} = 200$ nm and 310 nm, respectively. At approximately $\lambda = 1550$ nm, the phase is disturbed because the coupled resonance is excited. However, the phase converges to 0 far away from the resonant wavelength in both cases. Therefore, it can be concluded that $p = 1$ in both cases.

Table 1. Phase difference between the amplitudes of the two waveguide modes near the anti-crossing ($k_x = 0.1839[\pi/\Lambda]$) at the two coupled resonant modes ω_+ and ω_-. (a) $h_{\mathrm{metal}} = 200$ nm and (b) $h_{\mathrm{metal}} = 310$ nm.

(a) Phase difference for $h_{\mathrm{metal}} = 200$ nm

$[\arg(a_{TM1-}) - \arg(a_{TM0+})](\omega_+)$	$[\arg(a_{TM1-}) - \arg(a_{TM0+})](\omega_-)$	sign(α)	p
$5.982 \times 10^{-3}\pi$	1.001π	+	1

(b) Phase difference for $h_{\mathrm{metal}} = 310$ nm

$[\arg(a_{TM1-}) - \arg(a_{TM0+})](\omega_+)$	$[\arg(a_{TM1-}) - \arg(a_{TM0+})](\omega_-)$	sign(α)	p
1.001π	$-6.063 \times 10^{-2}\pi$	−	1

Sign(α) is evaluated based on the phase difference between the amplitudes at the two solutions of the coupled resonant mode with the upper (ω_+) and lower (ω_-) frequencies, as the coupled mode oscillation is viewed as the bonding or anti-bonding solution depending on the sign of the coupling constant α. The phase difference for $h_{\mathrm{metal}} = 200$ nm and 310 nm are summarized in table 1. For $h_{\mathrm{metal}} = 200$ nm, the two modes are in phase (out of phase) at ω_+ (ω_-), which corresponds to $\alpha > 0$, while for $h_{\mathrm{metal}} = 310$ nm, the two modes are out of phase (in phase) at ω_+ (ω_-), which corresponds to $\alpha < 0$. Therefore, we can conclude that $p\alpha$ is positive for $h_{\mathrm{metal}} = 200$ nm and negative for $h_{\mathrm{metal}} = 310$ nm, which confirms that the criteria of equation (9) are satisfied. We can also say that the sign($p\alpha$) is controlled by the grating thickness.

5. Variation of the anti-crossing gap and the emergence of exceptional point

5.1. Grating thickness dependence of the anti-crossing gap

In this section, we discuss the second feature of the device, namely the variation of the anti-crossing gap with the change of the grating thickness, h_{metal}. As seen in equation (8), the difference in the real part of the angular frequency Re$\{\Delta\omega\}$ between the non-BIC (radiating) and the BIC solutions is

$$\mathrm{Re}\{\Delta\omega\} = \frac{p\alpha}{2}\left(\sqrt{\frac{\gamma_{e1}}{\gamma_{e2}}} + \sqrt{\frac{\gamma_{e2}}{\gamma_{e1}}}\right). \tag{10}$$

Here, as mentioned above, $p = 1$ and sign(α) depends on h_{metal}. Although the radiation losses, γ_{e1} and γ_{e2}, are not exactly equal in our device, they are not much different, which can be observed from the linewidth of the two bright lines in figure 2. Therefore, we evaluate the value $p\alpha$ using an approximated relation $p\alpha = \Delta\omega$, where $\Delta\omega$ is evaluated based on the real part of the resonant-mode frequencies at $k_x = 0.185$ $[\pi/\Lambda]$, where the BIC appears. The result is shown in figure 6, where sign(α) was selected according to the result presented in section 4.3. The value of $p\alpha$ decreases as h_{metal} increases and crosses zero at approximately $h_{\mathrm{metal}} = 275$ nm.

5.2. Emergence of the exceptional point

Recently, with the same type of equation of motion as the TCMT (equation (2)) used above, the physics and the application of EPs in optics and photonics have been intensively investigated [35, 36]. Hence, it is interesting to consider the possibility of the realization of EP in the device considered here. The eigenfrequencies of the system are obtained [34, 57] as the solution of equation (6).

$$\omega = \frac{(\tilde{\omega}_1 + \tilde{\omega}_2) - \mathrm{i}(\gamma_{t1} + \gamma_{t2}) \pm \sqrt{D}}{2}, \tag{11}$$

where

$$D \equiv \{(\tilde{\omega}_1 - \tilde{\omega}_2)^2 - (\gamma_{t1} - \gamma_{t2})^2 + 4(\alpha^2 - \gamma_0^2)\} - i2\{(\tilde{\omega}_1 - \tilde{\omega}_2)(\gamma_{t1} - \gamma_{t2}) + 4\alpha\gamma_0\}. \tag{12}$$

The EP, where both the real and imaginary parts of the eigenfrequency coalesce, is realized when D becomes zero, i.e., Re$\{D\}$ = Im$\{D\} = 0$. Im$\{D\} = 0$ presents the following condition.

$$\omega_1 - \omega_2 = -\frac{4\alpha\gamma_0}{\gamma_{t1} - \gamma_{t2}} - p\alpha\left(\sqrt{\frac{\gamma_{e1}}{\gamma_{e2}}} + \sqrt{\frac{\gamma_{e2}}{\gamma_{e1}}}\right), \tag{13}$$

for which

$$\mathrm{Re}\{D\} = \frac{\{(\gamma_{t1} - \gamma_{t2})^2 + 4\gamma_0^2\}\{4\alpha^2 - (\gamma_{t1} - \gamma_{t2})^2\}}{(\gamma_{t1} - \gamma_{t2})^2} \tag{14}$$

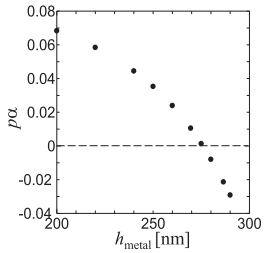

Figure 6. Value of $p\alpha$ as a function of the grating thickness calculated using equation (10). Here $p = 1$ and the sign(α) were selected in accordance with the result obtained in section 4.3.

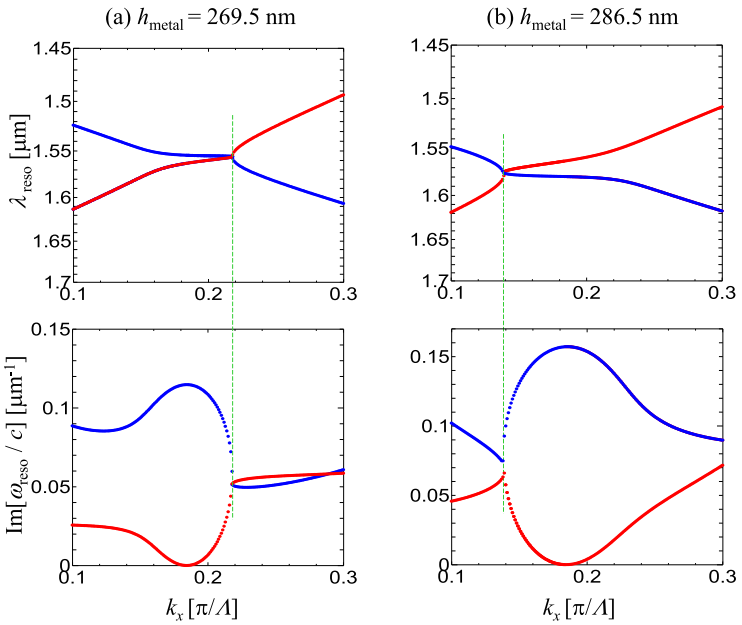

Figure 7. Real (upper) and imaginary (lower) parts of the coupled resonant modes for (a)$h_{\mathrm{metal}} = 269.5$ nm and (b)$h_{\mathrm{metal}} = 286.5$ nm. The real part is given by the corresponding wavelength. For each h_{metal}, there exists a point at which the real and imaginary parts coalesce, which indicates the EP.

becomes zero when $4\alpha^2 = (\gamma_{t1} - \gamma_{t2})^2$. The condition for the EP is then expressed as

$$|\gamma_{t1} - \gamma_{t2}| = 2|\alpha|, \tag{15}$$

$$\omega_1 - \omega_2 = \pm 2\gamma_0 - p\alpha\left(\sqrt{\frac{\gamma_{e1}}{\gamma_{e2}}} + \sqrt{\frac{\gamma_{e2}}{\gamma_{e1}}}\right) = p\sqrt{\gamma_{e1}\gamma_{e2}}\left\{\pm 2 - \alpha\left(\frac{1}{\gamma_{e2}} - \frac{1}{\gamma_{e1}}\right)\right\}. \tag{16}$$

In our device, $\omega_1 - \omega_2$ in equations (13) or (16) are selected based on k_x. The effect of the radiation loss $\gamma_{e1,2}$ and the radiation coupling γ_0 appears only in the form of the shift of the conditions.

Let us neglect the internal loss for the purpose of simplicity, i.e. $\gamma_{t1,2} = \gamma_{e1,2}$. Although it is difficult to evaluate precisely the values of $\gamma_{e1,2}$ in the specific structure, $|\alpha|$ can be tuned by changing the grating thickness h_{metal} as shown in figure 6. Therefore, we can identify a case where the EP emerges on varying h_{metal}. In figure 7, we show the dispersion relation of the resonant mode frequency for $h_{\mathrm{metal}} = 269.5$ nm and 286.5 nm, for which the coalescence of both the real and imaginary parts are observed at $k_x = 0.217[\pi/\Lambda]$ and $k_x = 0.140[\pi/\Lambda]$, respectively, thus demonstrating that the EPs are generated as expected. Although not demonstrated here, the EP does not appear for other h_{metal}. For the two cases of h_{metal} for which the EP is realized, α is evaluated based on figure 6 and the values of $\gamma_{e1,2}$ are then estimated by the fitting of the k_x-dependent eigenfrequencies of the TCMT to those of the CMM. The results are $\alpha/c = 0.01[1/\mu\mathrm{m}]$, $\gamma_{e1}/c = 0.05[1/\mu\mathrm{m}]$ and $\gamma_{e2}/c = 0.07[1/\mu\mathrm{m}]$ for $h_{\mathrm{metal}} = 269.5$ nm and $\alpha/c = -0.02[1/\mu\mathrm{m}]$, $\gamma_{e1}/c = 0.06[1/\mu\mathrm{m}]$ and $\gamma_{e2}/c = 0.1[1/\mu\mathrm{m}]$ for $h_{\mathrm{metal}} = 286.5$ nm, where c is the speed of light in vacuum. Therefore, in the present case, equation (16) is approximated as

$$\omega_1 - \omega_2 \simeq \pm 2\gamma_0, \tag{17}$$

which causes the EPs to appear at k_x in a manner nearly symmetrical with respect to the crossing point of the empty lattice modes, and hence, the BIC point, which is consistent with figure 7.

Equation (14) suggests that the eigenfrequencies have a split real part and degenerated imaginary part for $4\alpha^2 > (\gamma_{t1} - \gamma_{t2})^2$, which corresponds to the effective (passive) PT symmetric case and a split imaginary part and degenerated real part for $4\alpha^2 < (\gamma_{t1} - \gamma_{t2})^2$, which corresponds to the broken (effective) PT case [49], provided that equation (13) is satisfied. For the present device, we can observe the latter case for $269.5\ \text{nm} < h_{\text{metal}} < 286.5\ \text{nm}$ at a point between $0.217\ [\pi/\Lambda] > k_x > 0.140[\pi/\Lambda]$ and the former case outside these regions. Moreover, the structure presented here is suitable for the introduction of the gain as the pumping can be performed either optically through the slit or electrically through the grating and back metal. In either case of with or without gain, the tunability of the parameter α in our structure is expected to be useful in the control of the device. Lastly, we highlight that the control of α, which is realized in this study by controlling the grating thickness, can be realized using non-built-in methods. As discussed in section 4.1, the dependence of the resonant mode of the entire system and hence, α, on the grating thickness can be attributed to the change in the FP resonance in the slit. Therefore, we can expect that α can be varied by filling the slit with a dielectric or applying a voltage between the neighboring metal bars of the grating when the slit is filled with an electro-optical material. The latter method, if realized, would be particularly useful. On the other hand, the former method indicates a possibility of utilizing the device for the refractive index sensing. Further design considerations are necessary for both issues.

6. Conclusion

In this paper, we reported the emergence of the FW–BIC and EP in a dielectric waveguide comprising a metal grating, while focusing on their dependence on the grating thickness. For any grating thickness, the BIC emerges at one of the branches near the anti-crossing formed from the two waveguide modes TM_0 and TM_1 with internal (near field) and external (radiation) coupling via the slit of the grating. It was determined that, with a change in the thickness, the coupled modes move with the varying anti-crossing gap. The gap diminishes at a certain thickness and the branch at which the BIC appears flips. The change in the anti-crossing gap corresponds to the change in the internal coupling constant.

We showed that, when the slit is narrow to support single-mode propagation, the branch and position of the FW–BIC is determined by a simple rule: the FW–BIC appears in the vicinity of the crossing point between the two waveguide modes in the empty-lattice (zero slit-width) limit. In addition, these results are consistent with the criteria for the branch at which the BIC appears based on the phase of each basis mode presented in our previous paper. Owing to the dependence of the internal coupling on the grating thickness, we can find the cases in which the EP appears in the same device based only on the selection of the grating thickness, consistently with the prediction. As the dependence of the anti-crossing gap on the grating thickness can be understood in terms of the FP resonance in the slit, tuning could be performed using other methods such as the voltage applied to the metal grating with the slit filled by an electro-optical material. The BIC and EP in the dielectric waveguide comprising a metal grating, particularly with such tunability, are expected to result in the development of functional and high-performance optical and photonic devices as well as to become a platform for the fundamental research of non-Hermitian systems.

Funding

This work was supported by JSPS KAKENHI Grant Numbers JP18K04979 and JP18K04980.

Appendix A. Relation between the BIC position and the crossing point of the empty lattice bands

In this appendix, we analyze the relation between the BIC position and the crossing point of the empty lattice bands by comparing the results based on the rigorous coupled wave analysis (RCWA) method [59] and the CMM.

In the treatment of the CMM, all the effects of the grating are produced by the slit modes. The lowest order slit mode, TM_0, is a propagating mode that carries the energy from the resonant modes in the dielectric waveguide to the radiation in the air region. On the other hand, higher-order waveguide modes are evanescent in the narrow slits considered in this paper. In figure A1(a), we present the slit width dependence of the attenuation constants of the higher order slit modes, TM_1 (circles) and TM_2 (squares). It should be noted that the evanescent modes in the slit perforated in the real metal with finite permittivity ε_{m} will no longer be slit modes when the attenuation constant exceeds $\sqrt{-\varepsilon_{\text{m}}}\omega/c$, because the field will extend

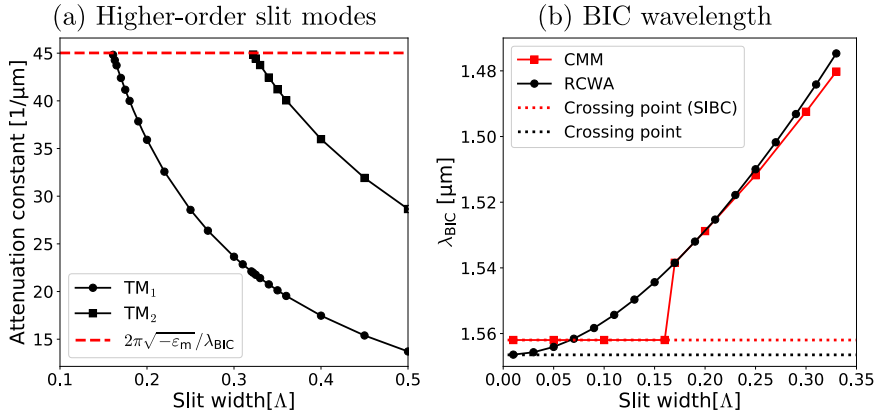

Figure A1. (a) Slit-width dependence of the attenuation constants of the higher order slit modes, TM_1 (circles) and TM_2 (squares). (b) Slit-width dependence of the BIC wavelength. The black and the red dotted lines indicate the wavelength of the crossing point of the empty lattice bands evaluated using the exact boundary condition for both of the metal/dielectric interfaces and using the surface impedance boundary condition (SIBC) for one of the interfaces, respectively.

on the whole metal surface. Therefore, only the lowest order TM_0 mode exists in the slit whose width is smaller than 0.17Λ.

The red squares in figure A1(b) depicts the slit width $w_s = \Lambda - w_m$ dependence of the BIC wavelength λ_{BIC} calculated using the CMM. We can see that the positions of the red squares for $w_s < 0.17\Lambda$ coincide perfectly with the red dotted line that depicts the wavelength of the crossing point of the empty lattice bands evaluated using the surface impedance boundary condition (SIBC) [60] for one of the metal/dielectric interfaces, although they are slightly shifted from the black dotted line that depicts the crossing point evaluated using exact boundary condition. This means that the small discrepancy between the BIC position and the crossing point observed in figure 3(a) is a result of the SIBC approximation used in the CMM calculation. Thus, the BIC position coincides basically with the crossing point of the empty lattice bands for the system with $w_s < 0.17\Lambda$ within the treatment of the CMM. However, when $w_s \geqslant 0.17\Lambda$, the BIC position is shifted discontinuously with the appearance of the evanescent slit mode TM_1. This behavior of the BIC position in our system is consistent with that in a quantum dot (QD) with attached leads discussed in [61]: the BIC position coincide with the crossing point of the nearest eigenenergies of the closed QD if all channels except the first propagating channel are disregarded, while there appears slight discrepancy due to the existence of the evanescent channels.

Apart from the treatment of the CMM, we find a difference in the slit-width dependence of the BIC position. The black circles in figure A1(b) depict the BIC wavelength obtained by the RCWA calculation, which indicate that there is a discrepancy between the BIC position and the crossing point even when $w_s < 0.17\Lambda$ and it grows continuously with the increase of the slit width. However, the results of the RCWA and the CMM are almost the same where $w_s \geqslant 0.17\Lambda$. This implies that a TM_1-like extended surface mode exists and contributes to the shift of the BIC position even when $w_s < 0.17\Lambda$, whose contribution is not included in the CMM formalism. In figures A2(a) and (b), we present the absorption maps calculated using the RCWA method for the systems with the slit widths $w_s = 0.1\Lambda$ and $w_s = 0.2\Lambda$, respectively. In both figures, the grating thickness h_{metal} is taken to be 100 nm. From figure A2(a), we can see that the shift of the BIC position obtained by the RCWA method is indeed larger than the shift obtained by the CMM shown in figure 3(a). From figure A2(b), we can see that the shift becomes remarkable as the slit width increases.

However, in any case, the shift is produced by the evanescent waves confined in the region of dozens of nm from the metal/dielectric interface. It is expected that the shift does not depend on the grating thickness unless it is small enough that the evanescent waves can penetrate it and contribute to the radiation, in which case, radiations from multiple modes coexist and the destructive interference between them can form a BIC, whose position may change exponentially depending on the grating thickness.

In figure A2(c), we show h_{metal} dependence of the BIC wavelength λ_{BIC} for the cases of $w_s = 0.1\Lambda$ (circles) and $w_s = 0.2\Lambda$ (triangles) calculated using the CMM (red marks) and the RCWA method (black marks). As we expected, the BIC positions are kept unchanged in the case the grating thickness is larger than 70 nm, while in the opposite case they change rapidly in the results of the RCWA calculation. The deviation of the results of CMM for $w_s = 0.2\Lambda$ in the region of $h_{metal} < 70$ nm can be attributed to the effect of direct tunneling through the metal region that is not included in the CMM calculation. In conclusion, although there is a slight discrepancy between the BIC position and the crossing point of the

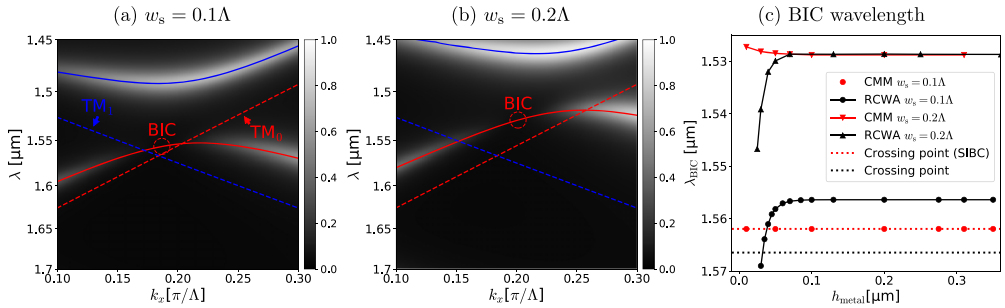

Figure A2. Absorption maps calculated using the RCWA method for the systems with the grating thickness of $h_{metal} = 100$ nm and the different slit sizes, (a) $w_s = 0.1\Lambda$ and (b) $w_s = 0.2\Lambda$. (c) h_{metal} dependence of the BIC wavelength for the cases of $w_s = 0.1\Lambda$ (circles) and $w_s = 0.2\Lambda$ (squares) calculated based on the CMM (red marks) and the RCWA (black marks). The dotted lines are the same as those depicted in figure A1(b).

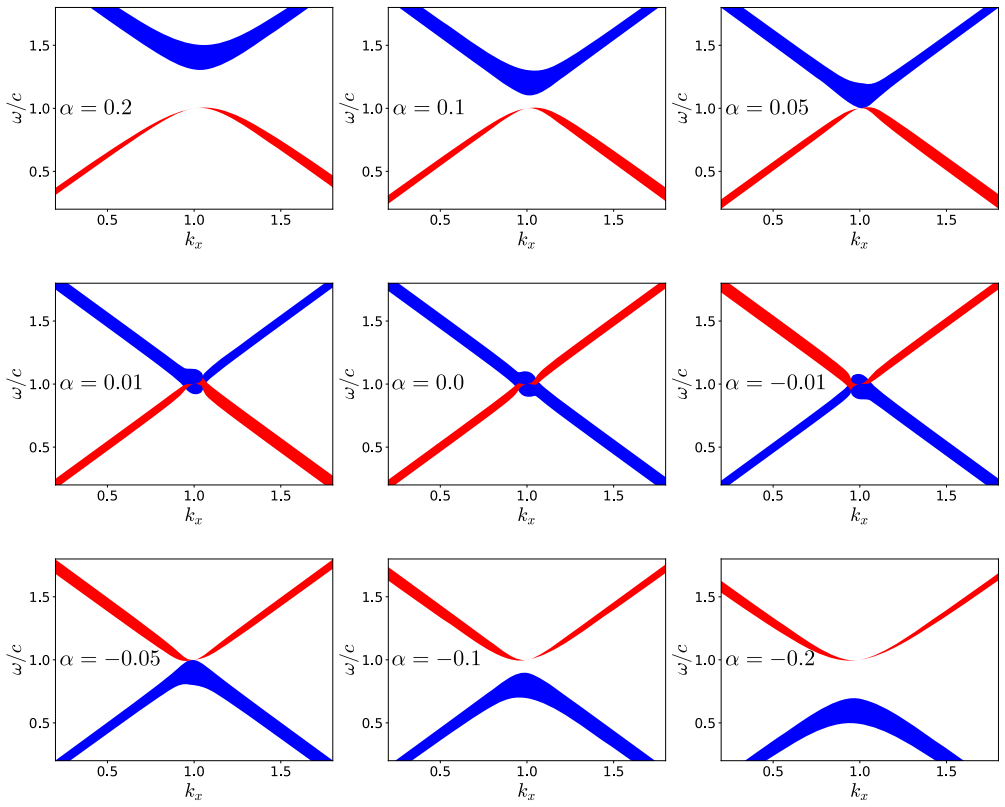

Figure B1. Dispersion relations of resonant modes for different α calculated using TCMT.

empty lattice bands, the position itself is kept unchanged during the inversion of the BIC branches if the grating thickness is larger than 70 nm.

Appendix B. Branch inversion of the BIC

In figure B1, we show the dispersion relations of resonant modes calculated using the TCMT developed in section 4.2. The half width of the lines is set to the imaginary part of the complex eigenfrequencies. Here, we assume the following dispersion relations for the original two modes

$$\omega_1 = \omega_0 + c(k_x - k_0), \tag{B.1}$$

$$\omega_2 = \omega_0 - c(k_x - k_0), \tag{B.2}$$

with $\omega_0/c = k_0 = 1.0$. We also assume $\gamma_1/c = 0.06$, $\gamma_2/c = 0.04$, $\gamma_{i1} = \gamma_{i2} = 0.0$ and $p = +1$. We can see that the positions of two branches are inverted when the sign of the coupling constant α changes and the behaviors of exceptional points discussed in section 5.2 appear around $\alpha = \pm 0.01$.

ORCID iDs

Munehiro Nishida https://orcid.org/0000-0003-2686-1442
Yutaka Kadoya https://orcid.org/0000-0001-6795-8115

References

[1] Hsu C W, Zhen B, Stone A D, Joannopoulos J D and Soljačić M 2016 Bound states in the continuum *Nat. Rev. Mater.* **1** 16048
[2] Koshelev K, Favraud G, Bogdanov A, Kivshar Y and Fratalocchi A 2019 Nonradiating photonics with resonant dielectric nanostructures *Nanophotonics* **8** 725–45
[3] von Neumann J and Wigner E 1929 Über merkwürdige diskrete Eigenwerte. Über das Verhalten von Eigenwerten bei adiabatischen Prozessen. *Z. Phys.* **30** 465–70
[4] Paddon P and young J E 2000 Two-dimensional vector-coupled-mode theory for textured planar waveguide *Phys. Rev.* B **61** 2090–101
[5] Christ A, Tikhodeev S G, Gippius N A, Kuhl J and Giessen H 2003 Waveguide-plasmon polaritons: strong coupling of photonic and electronic resonances in a metallic photonic crystal slab *Phys. Rev. Lett.* **91** 183901
[6] Shipman S P and Venakides S 2005 Resonant transmission near nonrobust periodic slab modes *Phys. Rev.* E **71** 026611
[7] Marinica D C, Borisov A G and Shabanov S V 2008 Bound states in the continuum in photonics *Phys. Rev. Lett.* **100** 183902
[8] Bulgakov E and Sadreev A F 2008 Bound states in the continuum in photonic waveguides inspired by defects *Phys. Rev.* B **78** 075105
[9] Dreisow F, Szameit A, Heinrich M, Keil R, Nolte S, Tünnermann A and Longhi S 2009 Adiabatic transfer of light via a continuum in optical waveguide *Opt. Lett.* **34** 2405–7
[10] Plotnik Y, Peleg O, Dreisow F, Heinrich M, Nolte S, Szameit A and Segev M 2011 Experimental observation of optical bound states in the continuum *Phys. Rev. Lett.* **107** 183901
[11] Lee J, Zhen B, Chua S-L, Qiu W, Joannopoulos J D, Soljačić M and Shapira O 2012 *Phys. Rev. Lett.* **109** 067401
[12] Hsu C W, Zhen B, Lee J, Chua S L, Johnson S G, Joannopoulos J D and Soljačić M 2013 Observation of trapped light within the radiation continuum *Nature* **499** 188–91
[13] Rybin M V, Koshelev K L, Sadrieva Z F, Samusev K B, Bogdanov A A, Limonov M F and Kivshar Y S 2017 High-Q supercavity modes in subwavelength dielectric resonators *Phys. Rev. Lett.* **119** 243901
[14] Zhang J, Kosugi Y, Otomo A, Nakano Y and Tanemura T 2017 Active metasurface modulator with electro-optic polymer using bimodal plasmonic resonance *Opt. Express* **25** 30304–11
[15] Kodigala A, Lepetit T, Gu Q, Bahari B, Fainman Y and Kant B 2017 Lasing action from photonic bound states in continuum *Nature* **541** 196–9
[16] Ha S T, Fu Y H, Emani N K, Pan Z, Bakker R M, Paniagua-Domnguez R and Kuznetsov A I 2018 Directional lasing in resonant semiconductor nanoantenna arrays *Nat. Nanotechnol.* **13** 1042–7
[17] Wang T and Zhang S 2018 Large enhancement of second harmonic generation from transition-metal dichalcogenide monolayer on grating near bound states in the continuum *Opt. Express* **26** 322–37
[18] Krasikov S D, Bogdanov A A and Iorsh I V 2018 Nonlinear bound states in the continuum of a one-dimensional photonic crystal slab *Phys. Rev.* B **97** 224309
[19] Carletti L, Koshelev K, De Angelis C and Kivshar Y 2018 Giant nonlinear response at the nanoscale driven by bound states in the continuum *Phys. Rev. Lett.* **121** 033903
[20] Minkov M, Gerace D and Fan S 2019 Doubly resonant $\chi^{(2)}$ nonlinear photonic crystal cavity based on a bound state in the continuum *Optica* **6** 1039–45
[21] Romano S, Zito G, Torino S, Calafiore G, Penzo E, Coppola G, Cabrini S, Rendina I and Mocella V 2018 Label-free sensing of ultralow-weight molecules with all-dielectric metasurfaces supporting bound states in the continuum *Photonics Res.* **6** 726–33
[22] Yesilkoy F, Arvelo E R, Jahani Y, Liu M, Tittl A, Cevher V, Kivshar Y and Altug H 2019 Ultrasensitive hyperspectral imaging and biodetection enabled by dielectric metasurfaces *Nat. Photon.* **13** 390–6
[23] Longhi S 2008 Transfer of light waves in optical waveguides via a continuum *Phys. Rev.* A **78** 013815
[24] Friedrich H and Wintgen D 1985 Interfering resonances and bound states in the continuum *Phys. Rev.* A **32** 3231–42
[25] Gao X, Hsu C W, Zhen B, Lin X, Joannopoulos J D, Soljačić M and Chen H 2016 Formation mechanism of guided resonances and bound states in the continuum in photonic crystal slabs *Sci. Rep.* **6** 31908
[26] Sadreev A F, Bulgakov E N and Rotter I 2006 Bound states in the continuum in open quantum billiards with a variable shape *Phys. Rev.* B **73** 235342
[27] Lepetit T, Akmansoy E, Ganne J-P and Lourtioz J-M 2010 Resonance continuum coupling in high-permittivity dielectric metamaterials *Phys. Rev.* B **82** 195307
[28] Lepetit T and Kant B 2014 Controlling multipolar radiation with symmetries for electromagnetic bound states in the continuum *Phys. Rev.* B **90** 241103
[29] Li L and Yin H 2016 Bound States in the continuum in double layer structures *Sci. Rep.* **6** 26988
[30] Bulgakov E N and Maksimov D N 2018 Avoided crossings and bound states in the continuum in low-contrast dielectric gratings *Phys. Rev.* A **98** 053840
[31] Azzam S I, Shalaev V M, Boltasseva A and Kildishev A V 2018 Formation of bound states in the continuum in hybrid plasmonic–photonic systems *Phys. Rev. Lett.* **121** 253901
[32] Kikkawa R, Nishida M and Kadoya Y 2019 Polarization-based branch selection of bound states in the continuum in dielectric waveguide modes anti-crossed by a metal grating *New J. Phys.* **21** 113020
[33] Heiss W D 2000 Repulsion of resonance states and exceptional points *Phys. Rev.* E **61** 929
[34] Eleuch H and Rotter I 2017 Resonances in open quantum systems *Phys. Rev.* A **95** 022117

[35] Miri M A and Alù A 2019 Exceptional points in optics and photonics *Science* **363** eaar7709
[36] Özdemir S K, Rotter S, Nori F and Yang L 2019 Parity-Time symmetry and exceptional points in photonics *Nat. Mater.* **18** 783–98
[37] Doppler J *et al* 2016 Dynamically encircling an exceptional point for asymmetric mode switching *Nature* **537** 76–80
[38] Hassan A U, Zhen B, Soljacic M, Khajavikhan M and Christodoulides D N 2017 Dynamically encircling exceptional points: exact evolution and polarization state conversion *Phys. Rev. Lett.* **118** 093002
[39] Feng L, Wong Z J, Ma R M, Wang Y and Zhang X 2014 Single-mode laser by parity-time symmetry breaking *Science* **346** 972–5
[40] Hodaei H, Miri M A, Heinrich M, Christodoulides D N and Khajavikhan M 2014 Parity-time symmetric microring lasers *Science* **346** 975–8
[41] Liu W, Li M, Guzzon R S, Norberg E J, Parker J S, Lu M, Coldren L A and Yao J 2017 An integrated parity-time symmetric wavelength-tunable single-mode microring laser *Nat. Commun.* **8** 15389
[42] Huang Y, Shen Y, Min C, Fan S and Veronis G 2017 Unidirectional reflectionless light propagation at exceptional points *Nanophotonics* **6** 977–96
[43] Huang Y, Min C and Veronis G 2016 Broadband near total light absorption in non-PT-symmetric waveguide-cavity systems *Opt. Express* **24** 22219–31
[44] Guo A, Salamo G J, Duchesne D, Morandotti R, Volatier-Ravat M, Aimez V, Siviloglou G A and Christodoulides D N 2009 Observation of PT-symmetry breaking in complex optical potentials *Phys. Rev. Lett.* **103** 093902
[45] Baum B, Lawrence M, Barton D III and Dionne J 2018 Active polarization control with a parity-time-symmetric plasmonic resonator *Phys. Rev.* B **98** 165418
[46] Lai Y H, Lu Y K, Suh M G, Yuan Z and Vahala K 2019 Observation of the exceptional-point-enhanced sagnac effect *Nature* **576** 65–71
[47] Hokmabadi M P, Schumer A, Christodoulides D N and Khajavikhan M 2019 Non-Hermitian ring laser gyroscopes with enhanced sagnac sensitivity *Nature* **576** 70–5
[48] Cerjan A, Hsu C W and Rechtsman M C 2019 Bound states in the continuum through environmental design *Phys. Rev. Lett.* **123** 023902
[49] Tuniz A, Wieduwilt T and Schmidt M A 2019 Tuning the effective PT phase of plasmonic eigenmodes *Phys. Rev. Lett.* **123** 213903
[50] Johnson P B and Christy R W 1972 Optical constants of the noble metals *Phys. Rev.* B **6** 4370–9
[51] Williams B S, Kumar S, Callebaut H and Hu Q 2003 Terahertz quantumcascade laser at $\lambda \approx 100$ μm using metal waveguide for mode confinement *Appl. Phys. Lett.* **83** 2124–6
[52] Garcia-Vidal F J, Martin-Moreno L, Ebbesen T W and Kuipers L 2010 Light passing through subwavelength apertures *Rev. Mod. Phys.* **82** 729–87
[53] Nishida M, Hatakenaka N and Kadoya Y 2015 Multipole surface plasmons in metallic nanohole arrays *Phys. Rev.* B **91** 235406
[54] Kikkawa R, Nishida M and Kadoya Y 2017 Substrate effects on the optical properties of metal gratings *J. Opt. Soc. Am.* B **34** 2578–85
[55] Fan S, Suh W and Joannopoulos J D 2003 Temporal coupled-mode theory for the Fano resonance in optical resonators *J. Opt. Soc. Am.* A **20** 569–72
[56] Suh W, Wang Z and Fan S 2004 Temporal coupled-mode theory and the presence of non-orthogonal modes in lossless multimode cavities *IEEE J. Quantum Electron.* **40** 1511–8
[57] Volya A and Zelevinsky V 2003 Non-Hermitian effective Hamiltonian and continuum shell model *Phys. Rev.* C **67** 054322
[58] Remacle F, Munster M, Pavlov-Verevkin V B and Desouter-Lecomte M 1990 Trapping in competitive decay of degenerate states *Phys. Lett.* A **145** 265–8
[59] Weiss T 2011 Advanced numerical and semi-analytical scattering matrix calculations for modern nano-optics *PhD Thesis* University of Stuttgart, Stuttgart
[60] Jackson J D 1999 *Classical Electrodynamics* 3rd edn (New York: Wiley)
[61] Bulgakov E and Sadreev A 2011 Formation of bound states in the continuum for a quantum dot with variable width *Phys. Rev.* B **83** 235321